Composites Science and Technology 135 (2016) 54–66

Contents lists available at ScienceDirect

Composites Science and Technology

journal homepage: http://www.elsevier.com/locate/compscitech

In-plane shear investigation of 3D surface-core braided composites

Jin Sun, Guangming Zhou*, Chuwei Zhou, Xinfeng Wang

State Key Laboratory of Mechanics and Control of Mechanical Structures, Nanjing University of Aeronautics and Astronautics, No. 29 Yudao Street, Nanjing 210016, China

ARTICLE INFO

Article history:
Received 3 May 2016
Received in revised form
3 July 2016
Accepted 12 September 2016
Available online 13 September 2016

Keywords:
Fibers
Mechanical properties
Stress/strain curves
Finite element analysis (FEA)

ABSTRACT

In-plane shear properties of three-dimensional (3D) surface-core braided composite are investigated by numerical simulation and experimental tests. Based on RVE models, the mechanical responses under in-plane shear load and the basic shear properties related to braiding parameters are predicted by using finite element method. Numerical results indicate that two groups of surface-cores possess distinct sensitivities to shear loads and identify the main load bearing components. In-plane shear tests are conducted to compare the effects of surface cuttings on the mechanical properties of present material and 3D 4-directional braided composite. The experimental data reveal that the cuttings degrade the shear moduli and strengths of the two materials to varying degrees. 3D surface-core braided composite can effectively restrain the decline of shear properties caused by cuttings. Scanning electron microscopy (SEM) is used to identify the distinct damage mechanisms of tested materials.

1. Introduction

Three-dimensional (3D) braided composites have been widely used as structural components for aircraft, rocket and other high-performance applications due to their excellent through-thickness reinforcement, high damage tolerance, favorable fatigue resistance and outstanding near-net-shape forming capacity [1–13]. However, one notable disadvantage of 3D braided composites is that their mechanical properties may easily degrade when they suffer surface damages, because their integrated fiber architecture can be seriously destroyed [14].

3D surface-core braided composite is a new material developed from traditional braided composites. The most significant improvement of this structure is that it can effectively limit the performance degradation caused by surface damages, depending on its particular "surface-core" structure. The effects of surface cuttings on longitudinal tensile properties of 3D surface-core and 3D 4-directional braided composites were experimentally compared [15]. The average tensile strength and modulus of new material dropped only 18 and 19% while those of 3D 4-directional braided composites with similar braiding angles and fiber volume fractions dropped 63 and 41%. Up to now, other basic mechanical behaviors of this new braided composite in certain conditions, such as in-plane shear loading, have not been reported, and it is necessary to carry out related research.

Currently, the studies on in-plane shear behavior of composite materials have been conducted by various test methods. E. H. Rani et al. [16] designed a modified Arcan fixture with butterfly specimen geometry to measure the in-plane shear response of thick-section pultruded FRP composites. Both the material shear stiffness and its nonlinear stress-strain response up to ultimate stress were determined. The specimen design minimized the stress concentrations at the edges, and allowed for approaching the nominal stress at the center. Results from strain gage and Infrared thermography measurements provided confirmation for the effectiveness of the fixture and the specimen geometry. D. O. Adams et al. [17] developed a V-notched rail shear test that incorporates the attractive features of both the Iosipescu test and the two-rail shear test. The V-notched specimen design reduces shear stress concentrations near the rails and produces relatively uniform shear stress distributions in the specimen gage section for a variety of carbon/epoxy laminates. Employing Iosipescu tests with a modified shear fixture, Guo et al. [18] investigated the evolution of the in-plane shear damage and the stress–strain behaviors of a two-dimensional Hi-Nicalon fibre-reinforced silicon carbide composite (2D-SiC/SiC) under monotonic, non-reverse and reverse cyclic load conditions. Liang et al. [19] compared the nonlinear in-plane shear properties of unidirectional fiber reinforced composites and fabric reinforced composites by $\pm 45^{\circ}$ tension tests. The experimental results revealed that fabric reinforced composite showed more

* Corresponding author.
E-mail address: zhougm@nuaa.edu.cn (G. Zhou).

http://dx.doi.org/10.1016/j.compscitech.2016.09.011

ductile-like response in the preyield phase and better load bearing ability in the post-yield phase compared to the unidirectional fiber reinforced composite. Li et al. [20] characterized the in-plane shear behavior of non-crimp fabrics (NCFs), including NCFs based on T300 carbon fibers with chain or tricot-chain stitches by picture frame and bias extension tests. The normalized results of these two tests for shear force are consistent with each other in the direction of shear of the stitching, while deviations in other directions are attributed to the different strain mechanisms, as a result of the clamping way of the sample in the test. A. C. Manalo et al. [21] conducted an asymmetrical beam shear test to determine the behavior of fiber composite sandwich beams under in-plane shear loading. The experimental results showed a good agreement with theoretical prediction, and the asymmetrical shear test was recommended as a test method for determining the shear properties of sandwich structures with high strength core materials.

The objective of this paper is to investigate the in-plane shear properties of 3D surface-core braided composite and its particular superiority over traditional braided composites when they all suffer surface damage. Firstly, the finite element method is employed to present the mechanical response of established RVE models. The stress distribution with significant characteristics identifies the primary load bearing components, which indicates the possibility that the shear properties will not remarkably degrade if the surface damages do not destroy these components. Meanwhile, the basic shear properties related to braiding parameters are characterized by using homogenization approach and volume averaging method. Secondly, the in-plane shear tests are conducted to compare the effects of surface cuttings on the shear properties of present material and traditional braided composite. The shear properties of undamaged and pre-damaged 3D surface-core and 3D 4-directional braided composites are measured by Arcan method, respectively. The stress-strain behaviors, shear moduli, shear strengths, failure modes and damage mechanisms of these two materials including four configurations are contrasted in detail. Both the numerical and experimental studies fill the gap in the in-plane shear investigation of 3D surface-core braided composite, which could give us new insights into the performance of this new material.

2. Braiding process

Fig. 1(a) demonstrates the permutation and movement of carriers on a machine bed. The carriers can be divided into two orthogonal systems. Every two rows or columns constitute a moving sub-block in x or y direction. The braiding process is composed of alternate two steps. At step 1, the carriers in x directional sub-blocks move clockwise one position. At step 2, the carriers in y directional sub-blocks move counterclockwise one position. Each step is followed with a ‘jamming’ action. The unit length of the resultant preform is defined as the braiding pitch, denoted by h.

Repeating above steps, all the yarns in one sub-block are continuously prolonged along their spatial traces, and a ‘surface-core’ is finally formed. The number of surface-cores in x or y direction is denoted by m or n. The size of 3D surface-core braided preform is denoted by (m, n).

3. Finite element analysis

3D surface-core braided composite has a skin-core structure, as shown in Fig. 1(b). For studying the material with periodic microstructure, the representative volume element is usually picked out and analyzed instead of the whole structure. Based on the braiding process and the spatial configuration of braiding yarns located in

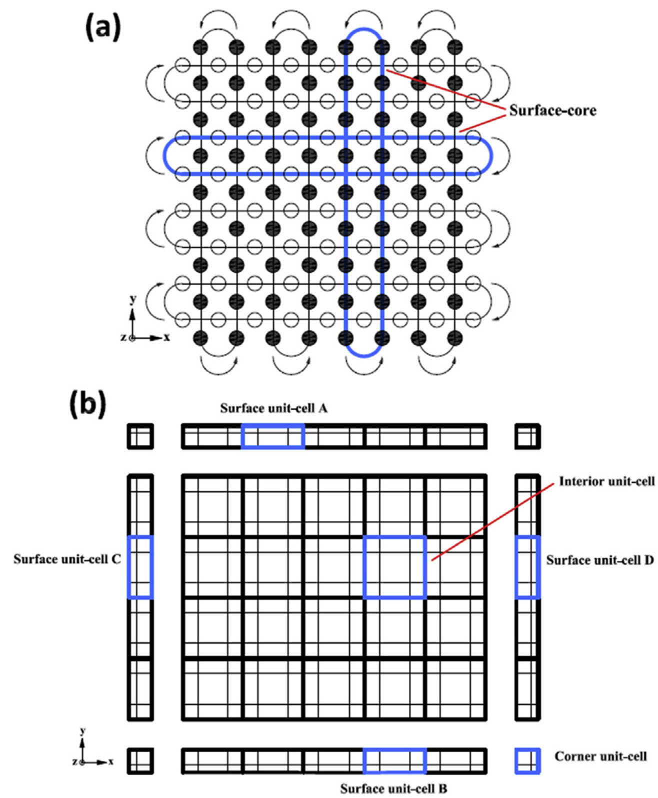

Fig. 1. Structure description of 3D surface-core braided composites: (a) Braiding process and (b) unit-cell division.

the interior, surface and corner regions, three unit-cell models were proposed in Ref. [15]. Fig. 2 demonstrates the solid structure models of unit-cells. Considering the mutual squeezing of yarns is more obvious due to the abrupt change of the yarn paths in the exterior regions, the cross section of interior yarns is assumed to be a hexagon inscribed with an ellipse which is regarded as the cross section of yarns in exterior regions. The relationship between the major and minor radii of the ellipse, a and b, is expressed as $a = \sqrt{3}b \cos \gamma$. The gradual change of the yarn's cross section shape from the exterior regions to the interior is neglected.

In this study, the size of investigated 3D surface-core braided preforms is (2, 14). The interior unit-cells and surface unit-cells A and B account for 50.0 and 43.7% of the whole structure, respectively. The corner unit-cells and surface unit-cells C and D occupy a small part of the material, and are neglected for the finite element analysis.

3.1. Finite element modeling

3D surface-core braided composites are composed of braiding yarns and resin matrix. In this work, the braiding yarns containing thousands of fibers and matrix are regarded as unidirectional composites and are modeled as transversely isotropic material in local coordinate system. The resin matrix is assumed to be isotropic. The elastic properties of component materials are listed in Table 1. The elastic properties of braiding yarns are calculated by the micromechanics formulae proposed by Chamis [22].

The 4-node linear tetrahedron element (C3D4) available in ABAQUS is used for free mesh generation depending on its outstanding geometry boundary adaptability. The general periodic boundary conditions which can realize the application of periodic boundary conditions with aperiodic mesh are adopted [23]. In

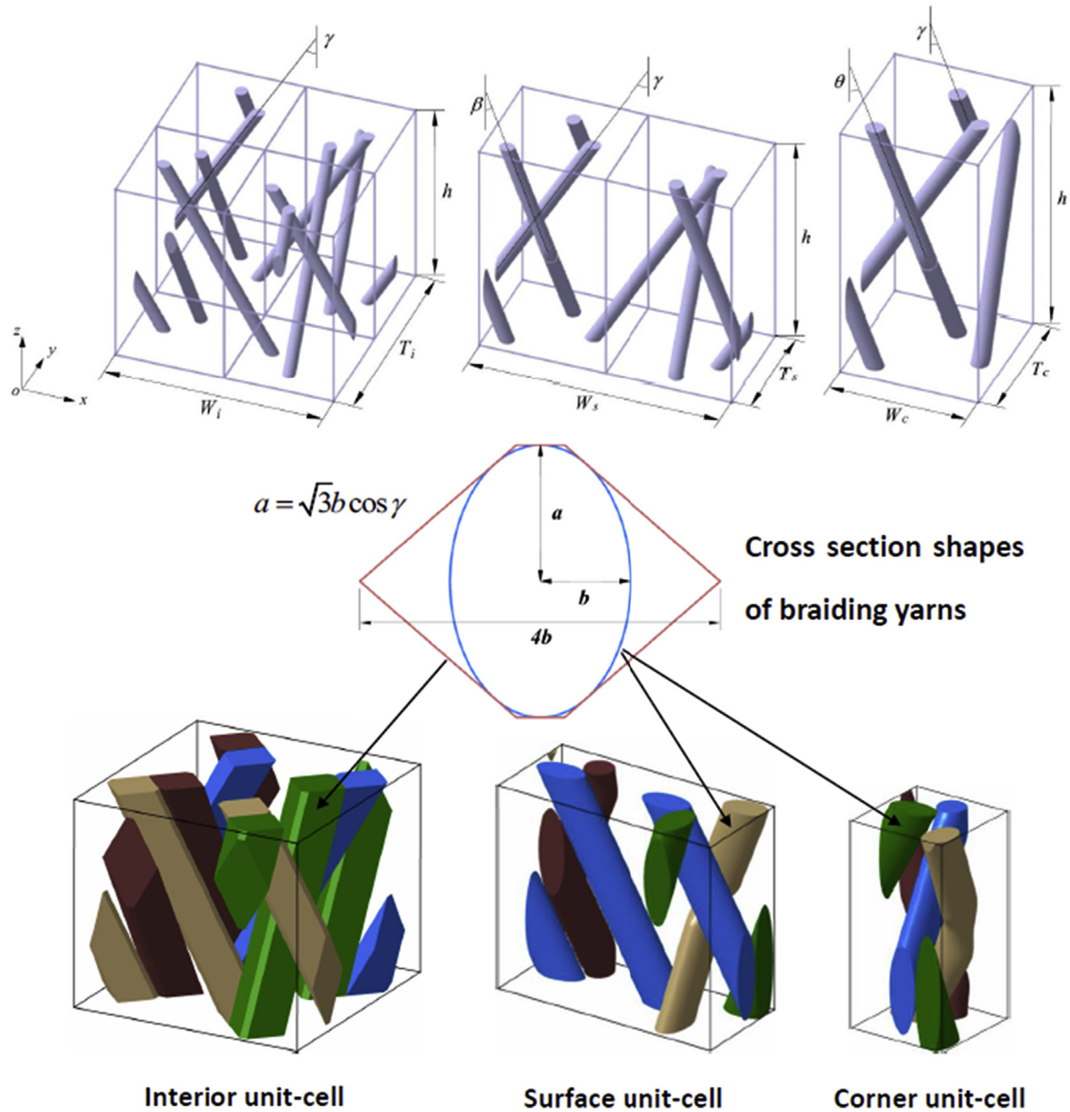

Fig. 2. Solid structure models of three unit-cells.

order to satisfy the continuities of stress and displacement on the interfaces between the component materials, the merged coincident meshes are adopted on the interfaces.

To simulate the in-plane shear load case, an independent set of global strain, namely, $[\bar{\varepsilon}_x, \bar{\varepsilon}_y, \bar{\varepsilon}_z, \bar{\gamma}_{yz}, \bar{\gamma}_{zx}, \bar{\gamma}_{xy}] = [0, 0, 0, 0, 0.002, 0]$, is applied in finite element models. The shear load is imposed by displacement which is determined by input global strain and boundary dimension of the model. The displacement load combined with corresponding boundary constraints can simulate in-plane shear load case, as shown in Fig. 3. Corresponding to this load case, the displacement load and the constraints by relative displacement between opposite boundary surfaces of unit-cell are expressed by

$$\left\{\begin{array}{ll} \left(\begin{array}{l} u_{CDHG} - u_{BAEF} = 0 \\ v_{CDHG} - v_{BAEF} = 0 \\ w_{CDHG} - w_{BAEF} = w_C - w_B = w_C \end{array}\right. & \left(\begin{array}{l} u_{GHEF} - u_{CDAB} = u_F - u_B = u_F \\ v_{GHEF} - v_{CDAB} = 0 \\ w_{GHEF} - w_{CDAB} = 0 \end{array}\right. \\ \left(\begin{array}{l} u_{DAEH} - u_{CBFG} = 0 \\ v_{DAEH} - v_{CBFG} = 0 \\ w_{DAEH} - w_{CBFG} = 0 \end{array}\right. & \left(\begin{array}{l} u_B = v_B = w_B = u_A = v_A = w_A = 0 \\ u_C = v_C = v_F = w_F = 0 \\ w_C = \bar{\gamma}_{xz} W_k, u_F = \bar{\gamma}_{xz} h \end{array}\right. \end{array}\right. \quad (k = i, s)$$

where u, v and w are the displacements in x, y and z directions, respectively; W is the width of unit-cell and the subscript i and s refer to the interior and surface unit-cells.

Global coordinate system is adopted by the interior unit-cell and surface unit-cell A. Due to the antisymmetry of the structure, the

Table 1
Mechanical properties of fiber and resin.

Material components	Young's modulus (GPa)	Shear modulus (GPa)	Poisson's ratio
E-glass fiber	73.0	30.0	0.22
Epoxy resin	3.5	1.3	0.35

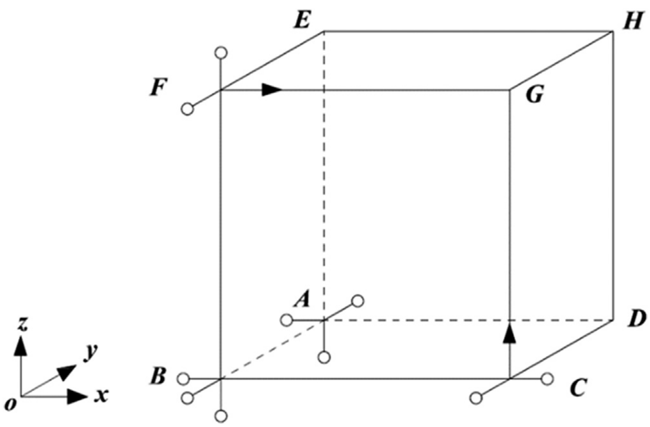

Fig. 3. Displacement loads and boundary constraints under in-plane shear load.

simulation of surface unit-cell B is realized by applying inverse loads on surface unit-cell A and adopting a local coordinate system in which the *x* and *y* axes are contrary to those in global coordinate system.

3.2. Mechanical response of unit-cells

When a shear load is applied on a composite, it is not directly imposed on the fibers but firstly on the resin matrix. The fibers achieve the shear load from the matrix by stress transfer and produce stresses to balance the load. The axial stress is the main type of the born stresses of fibers, thus more attention should be paid to it. The following will present the mechanical response of unit-cells with interior braiding angle of 30° by their deformation and stress distribution, respectively.

Fig. 4 displays the deformation of unit-cells when the deformation scale factor is 200. It is seen that the boundary surfaces of unit-cells are warped. Each pair of opposite boundary surfaces have the same deformation which guarantees the displacement continuity between the neighboring unit-cells and provides a reasonable stress distribution. The warping extents of three sets of opposite boundary surfaces are distinct, which is attributed to that the unit-cell model of 3D surface-core braided composites does not have the symmetries of geometrical structure and physical properties.

Fig. 5 shows the stress nephogram of interior unit-cell. The stress continuity at the opposite boundary surfaces has been guaranteed and satisfied the periodic condition. Fig. 5 (a)-(c) describes the Mises stress distribution of the whole model, resin matrix and yarns, respectively. It is seen that the yarns inclining to *x* direction rather than *y* direction bear the primary load. The stresses in main load-carrying yarns are more 8 times than those in resin matrix on the average, which indicates that these yarns are the main load bearing component for the composites. The stress concentration is distributed in the interlaced region of braiding yarns and the contact area between yarns and matrix. The closer to these regions, the greater stresses are produced. Fig. 5 (d) depicts the 1st directional stress nephogram of the yarns. Since the yarns are modeled as transversely isotropic material in local coordinate system, the 1st directional stress indicates the axial stress for each yarn. The regions with positive value bear tensile stress while those with negative value bear compressive stress. It is seen that the yarns inclining to positive *x* direction bear tensile stress while those inclining to negative *x* direction bear compressive stress. Whether tensile stresses or compressive stresses in the yarns along *y* direction, are far lower than those in the yarns along *x* direction.

Figs. 6 and 7 present the stress nephogram of surface unit-cells A and B. The stress continuity at the opposite boundary surfaces has still been guaranteed. Fig. 6 (a)-(c) and Fig. 7 (a)-(c) show the Mises stress distributions of the two surface unit-cells. For both of them, the primary loads are born by *x* directional yarns in which the stresses are more 7 times than those in matrix on the average. The abrupt changes of yarn paths lead to severer mutual squeezing of yarns, causing obvious stress concentrations in their interlaced areas. Fig. 6 (d) and Fig. 7 (d) depict the 1st directional stress (axial stress) nephogram of yarns. It should be noted that the *x* and *y* axes in local coordinate system of surface unit-cell B are inverse to those in global coordinate system. Accordingly, the yarns inclining to positive *x* direction (Global CS) bear tensile stress while those inclining to negative *x* direction (Global CS) bear compressive stress, and the stresses in the yarns along *y* direction are far weaker than those in *x* directional yarns.

The stress nephogram can only describe the mechanical response in a qualitative way by supplying the information about stress distribution mainly on the surfaces or certain cross sections [24]. To quantitatively demonstrate the stress everywhere, particularly in the interior of yarns, the cumulative sum of elements

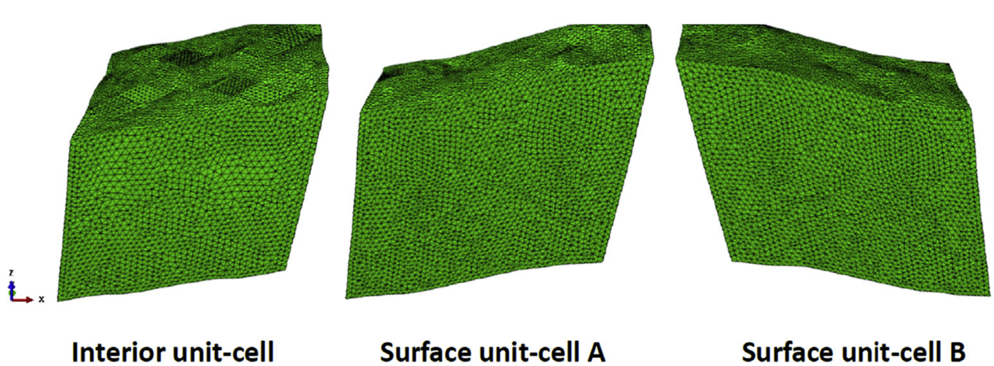

Fig. 4. Deformation of the finite element models under in-plane shear load.

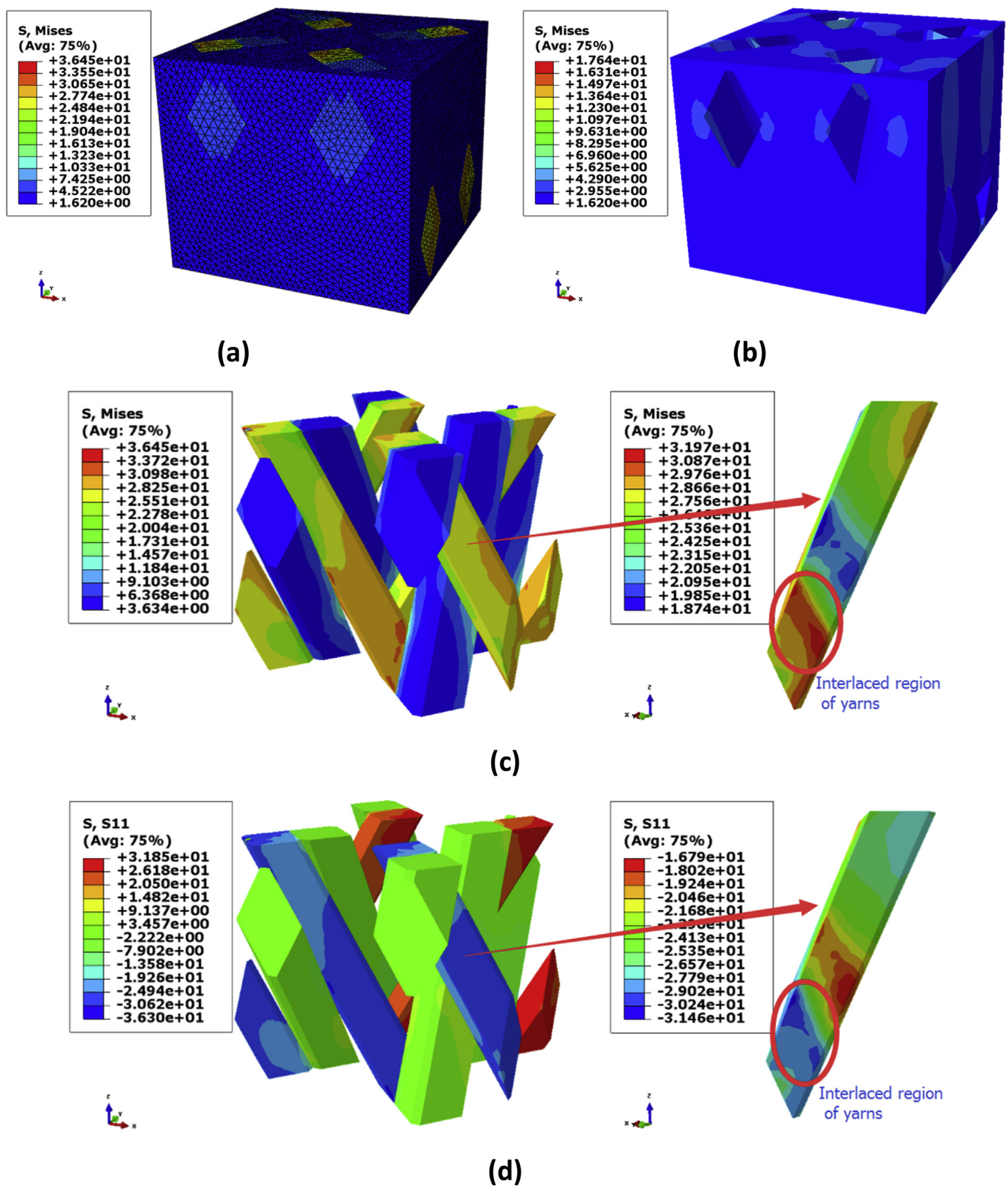

Fig. 5. Stress nephogram of interior unit-cell: Mises stress distribution of (a) whole model, (b) resin matrix and (c) braiding yarns, and (d) axial stress distribution of braiding yarns.

volume with increasing stress level is counted according to the stress and volume data of each element, which can determine what percentage of the yarns exceeds a certain stress level. Since the loads of finite element models are given artificially, which leads to corresponding stress values, the obtained stresses are non-dimensionalized by mean stress herein. For the axial stresses of yarns, $\overline{\sigma}_{axial}$ is defined as their average value and is expressed by

$$\overline{\sigma}_{axial} = \frac{1}{V}\int_V |\sigma_{axial}| \mathrm{d}V \tag{2}$$

where σ_{axial} indicates the 1st directional stress (axial stress for yarns) of each element and V the volume of total yarns in a unit-cell.

To further compare the load bearing characteristics of yarns inclining to distinct directions, the yarns are divided into two groups. The Group 1 and Group 2 represent the yarns inclining to x direction and y direction, respectively. The relationships between stress level and volume proportion of yarns in these two groups for three unit-cells are shown in Fig. 8. The more the curve increases in a certain range of stress level, the more the yarn volumes are distributed in this region. It is seen that the yarns of Group 1 are distributed at obviously higher stress levels (including tensile and

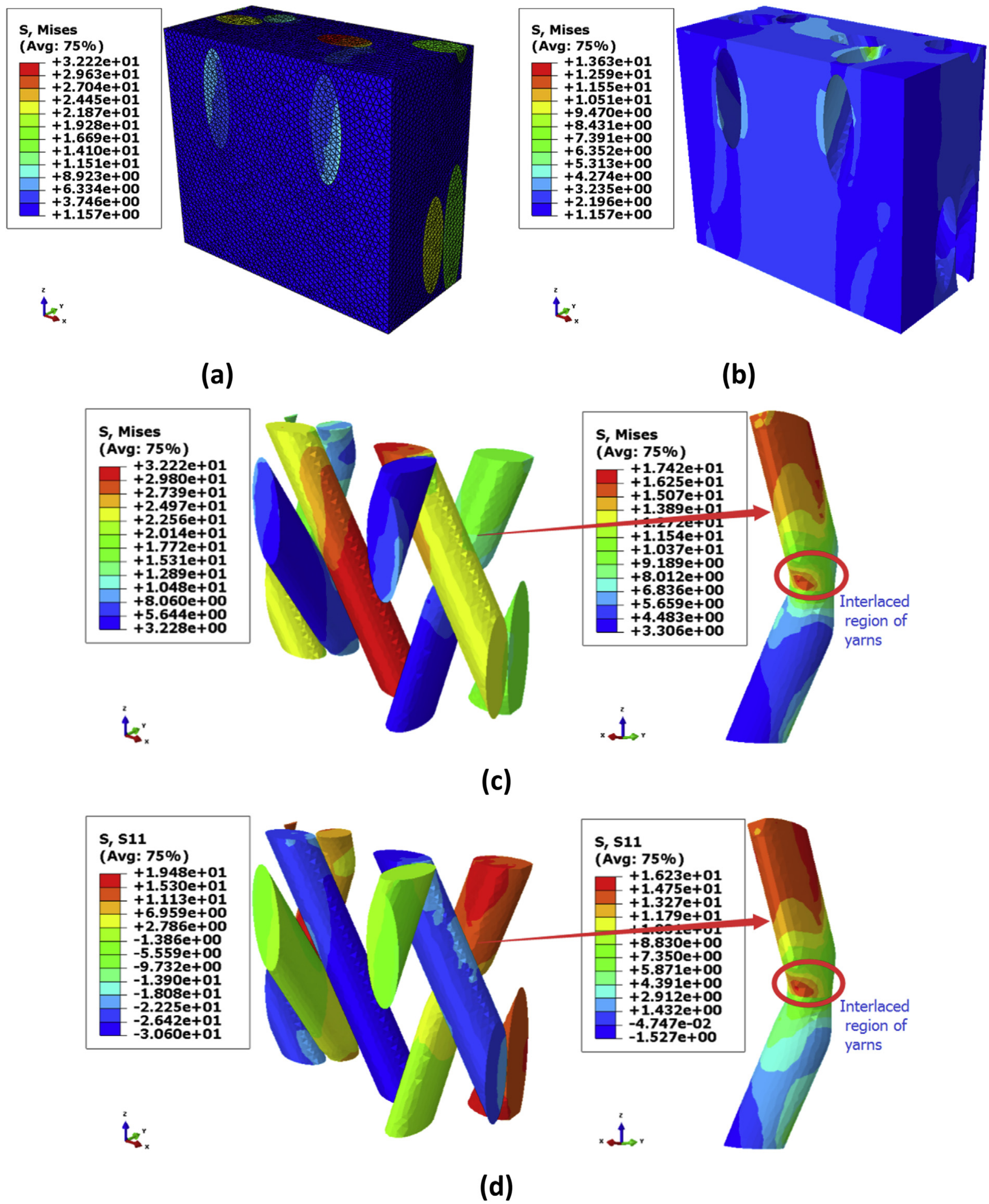

Fig. 6. Stress nephogram of surface unit-cell A: Mises stress distribution of (a) whole model, (b) resin matrix and (c) braiding yarns, and (d) axial stress distribution of braiding yarns.

compressive stresses) than those of Group 2 for all three unit-cells. Nearly 50% of Group 1 yarns in the interior unit-cell are distributed from 1.5 to 2.2 times the mean stress and also nearly 50% from -2.2 to -1.5 times the mean stress. The yarns in these two stress intervals incline to positive and negative x direction, respectively. Between the two intervals, the curve of Group 1 undergoes a flat stage, which indicates no Group 1 yarn is distributed in this stress range. Besides, all yarns of Group 2 are distributed between the stress levels of -1 and 1, and most of them are close to 0, which means the stresses in these yarns are far less than the mean stress. For the surface unit-cell A, about 40% of Group 1 yarns are distributed from only 0.5 to 1.2 times the mean stress, while up to 60% from -2 to -1.3 times the mean stress, which indicates the Group 1 yarns do more contributions to bearing compressive stress. Conversely, about 60% of Group 1 yarns in surface unit-cell B are distributed from 1.3 to 2 times the mean stress, while nearly 40%

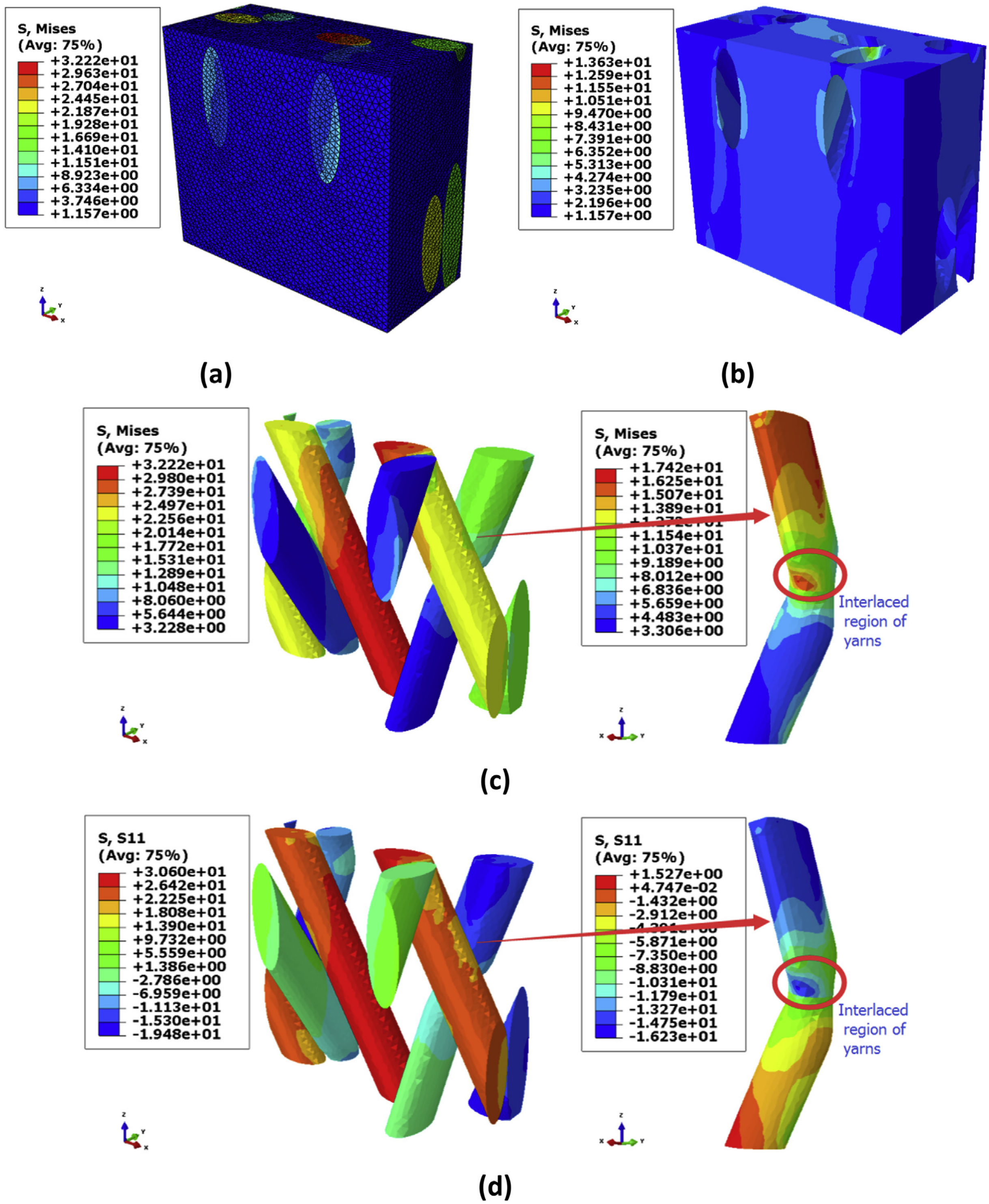

Fig. 7. Stress nephogram of surface unit-cell B: Mises stress distribution of (a) whole model, (b) resin matrix and (c) braiding yarns, and (d) axial stress distribution of braiding yarns.

from −1.2 to −0.5 times the mean stress, which reflects the yarns of this group mainly bear tensile stress. In addition, the stresses of Group 2 yarns in both the surface unit-cells A and B are still much lower than the mean stress.

From above, the yarns inclining to x direction bear obviously more stresses than those inclining to y direction. In other words, the surface-cores parallel to the specimen surface rather than the ones perpendicular to it are the primary load carrying components under in-plane shear loads. When 3D surface-core braided composites suffer surface cuttings, the surface-cores perpendicular to material surface will be damaged while those parallel to it will still maintain their integrality. Accordingly, it can be predicted that since the main load bearing components of the material are not destroyed by surface cuttings, its in-plane shear properties will not significantly degrade. This prediction will be verified by mechanical tests introduced in Section 4.

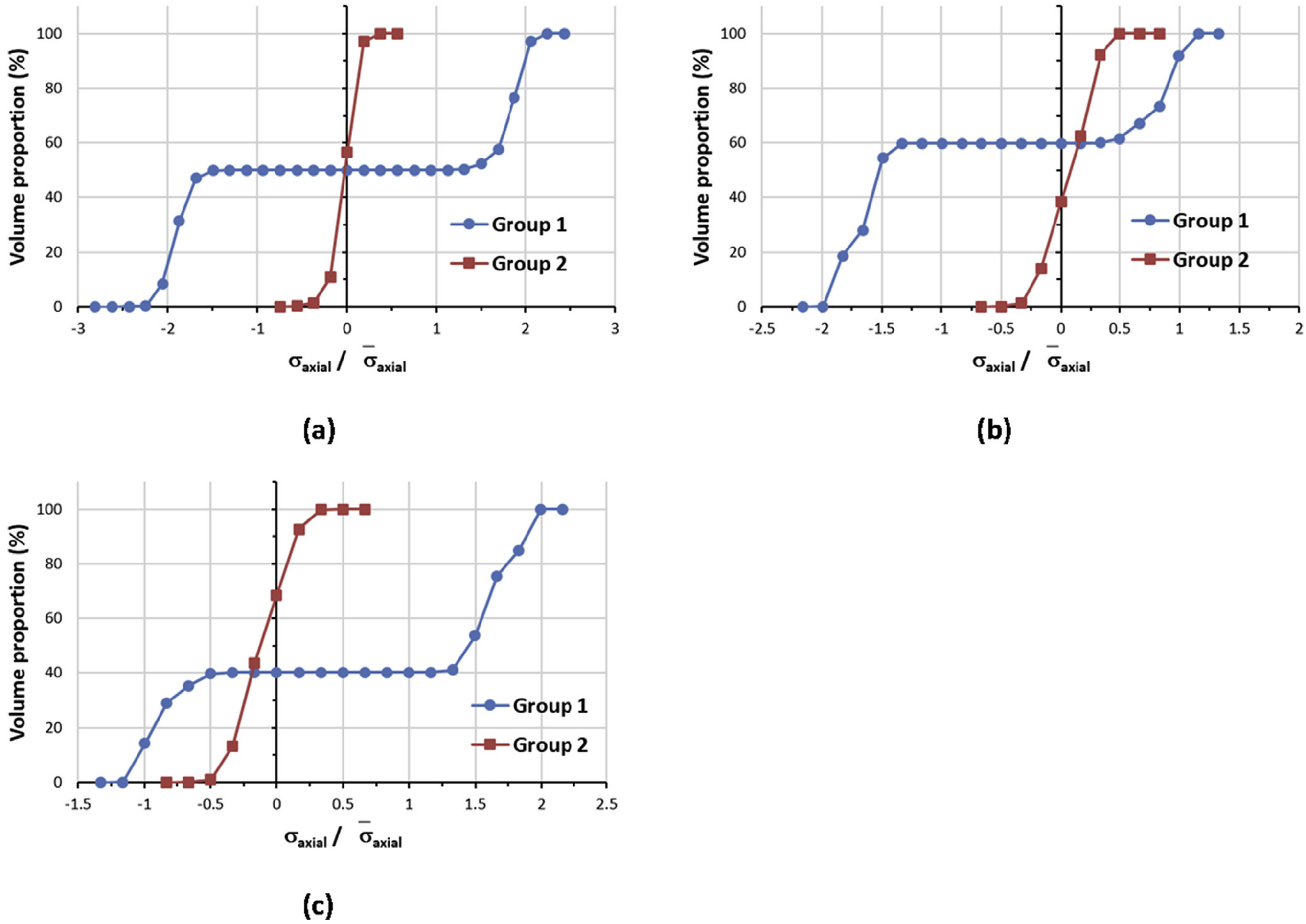

Fig. 8. Relations between nondimensionalized axial stress and volume proportion of yarns for (a) interior unit-cell, (b) surface unit-cell A and (c) surface unit-cell B under in-plane shear loads.

3.3. Discussion on braiding parameters

According to the mechanical response of each unit-cell, the effective in-plane shear properties of whole composite can be obtained by homogenization approach and volume averaging method [25–27]. The effects of two braiding parameters, namely braiding angle and fiber volume fraction, on shear modulus are studied herein.

Fig. 9 shows the variation of predicted in-plane shear modulus G_{xz} with braiding angle under three different fiber volume fractions. It is seen that G_{xz} firstly increases steadily as the braiding angle grows. When the braiding angle is greater than 35°, the increment becomes smaller. At the braiding angle of 45°, G_{xz} reaches the peak value. Besides, G_{xz} goes up with the increase of fiber volume fraction, and the increment is relatively significant when the braiding angle is large.

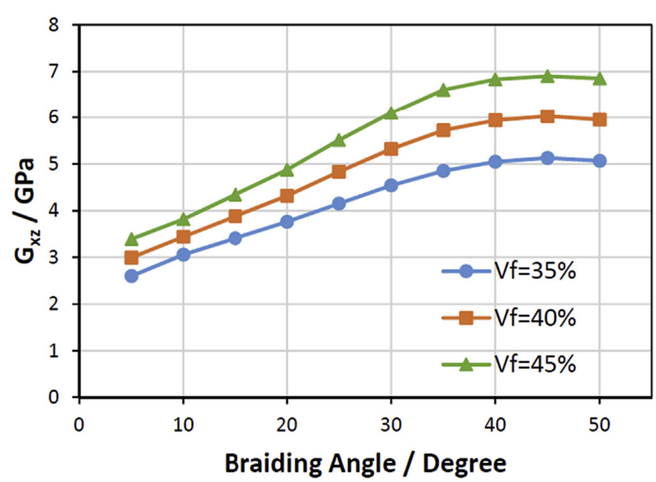

Fig. 9. Variation of shear modulus with braiding angle and fiber volume fraction.

4. Experimental program

To investigate the in-plane shear properties of 3D surface-core braided composite, especially its superiority over the traditional braided composites when they all suffer surface damage, the specimens of this new material and 3D 4-directional braided composite were prepared and the V-notched beam shear tests were performed.

4.1. Materials and specimens

The reinforcement fiber for both the 3D surface-core and 3D 4-directional braided preforms was E-glass fiber. The sizes of 3D surface-core preforms contained (2, 14) and (4, 14). The latter was used for surface cuttings. The preforms were consolidated into the

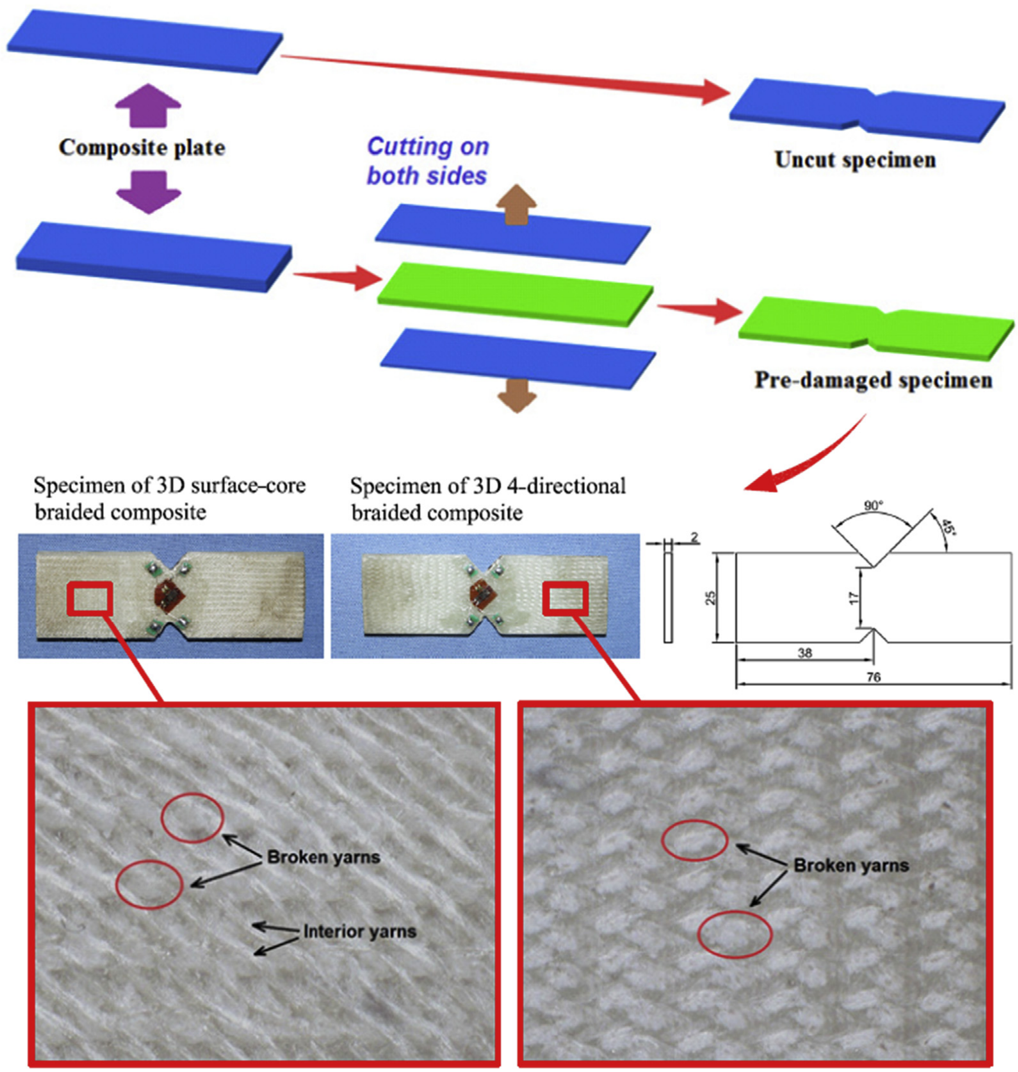

Fig. 10. Dimensions and surface morphology of specimens.

final composites by impregnating with epoxy resin using RTM process. The mechanical properties of the fiber and resin have been given in Table 1. The pre-damaged specimens were processed by cutting on both sides of the composites.

Fig. 10 shows the dimensions and actual surface morphology of specimens. It is seen that the surface cuttings produced plenty of broken yarns whose fracture sections were regularly distributed on specimen surfaces of both the materials. In detail, the specimen surface of 3D 4-directional braided composite was completely filled with yarn fracture sections, since the spatial trace of each yarn was not parallel with the boundary of specimen but throughout its thickness, and all the yarns were cut off when they reached the cut surface. In contrast, although broken yarns existed, plenty of intact interior yarns were observed on the specimen surface of 3D surface-core braided composite. Actually, the broken yarns were produced by the surface-cores perpendicular to specimen surface, and the intact yarns belonged to the adjacent surface-core parallel to the specimen surface. Surface cuttings removed the superficial surface-cores on both sides of specimen, but the left ones parallel to cut surface well kept their integrality, which was the key to maintain mechanical properties. The effect of surface cuttings on shear properties of 3D surface-core braided composites has been preliminarily predicted in the last paragraph of Section 3.2. The following tests will minutely investigate how this damage influences the in-plane shear properties of the material.

4.2. Experimental

The specimens were loaded in a MTS 370.25 test machine by a modified Arcan test fixture at a constant head speed of 1 mm/min, as shown in Fig. 11. The strain gauges (Micro-Measurement type BE120-3BC from ZEMIC, China) bonded in the middle of the specimen measured strain oriented at ±45° to the loading axis (denoted by$\varepsilon_{\pm 45}$) to determine the shear response during the entire loading procedure. The shear strain was then obtained from the strain gauges by

$$\gamma = \varepsilon_{+45} - \varepsilon_{-45} \tag{3}$$

The shear stress was determined by

$$\tau = \frac{P}{A} \tag{4}$$

where P is the applied load, and A is the area of the cross section between the notches. The apparent shear modulus was then calculated by

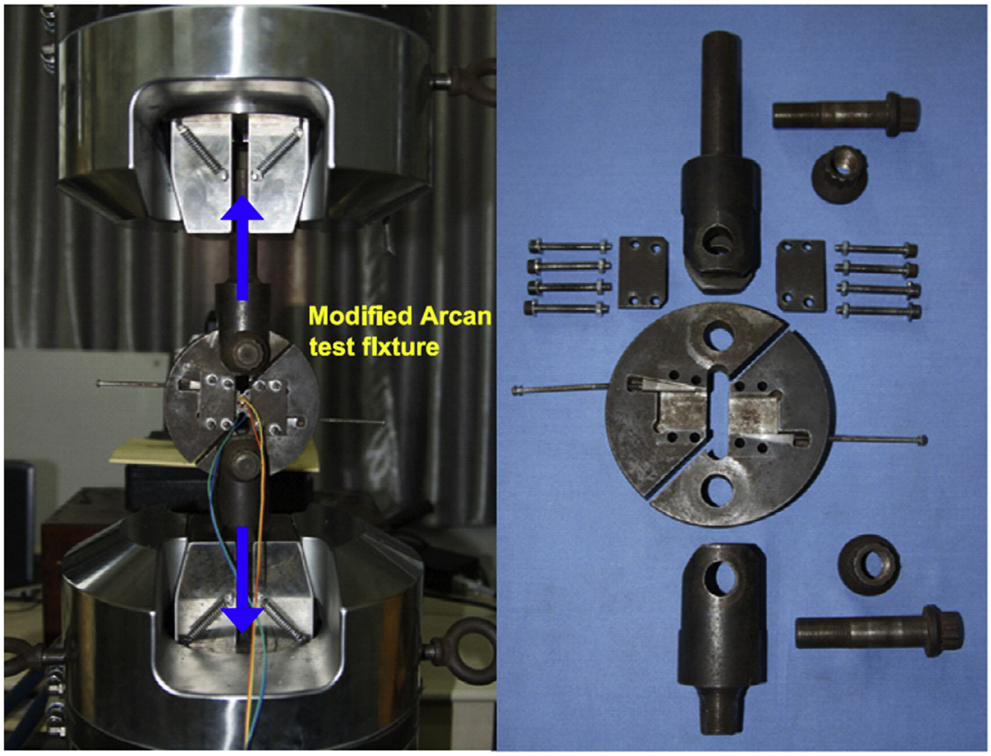

Fig. 11. Test fixture for in-plane shear test.

$$G = \frac{\tau}{\gamma} \tag{5}$$

4.3. Experimental results and discussion

4.3.1. Stress-strain behaviors

The in-plane shear stress-strain behaviors of 3D surface-core and 3D 4-directional braided composites under shearing load are shown in Figs. 12 and 13. The strains oriented at ±45° to the loading axis and shear strains for uncut and cut specimens are simultaneously depicted in the figures. The initial elastic stress-strain behaviors can be observed in all curves, and then the nonlinear behaviors appear sooner or later and become more significant with increasing stress due to the occurrence and accumulation of shear damage.

From Figs. 12 and 13, all curves of uncut specimen show a larger linear range and reach a higher ultimate stress than corresponding ones of cut specimen. For 3D surface-core braided composites, the shear stress-strain curve of uncut specimen shows a linear phase up to about 1.3% strain followed with a nonlinear region which reaches the peak value at approximately 2.3% strain. In comparison, the shear stress-strain curve of cut specimen shows a shorter linear phase up to less than 0.7% strain with a relatively small slope, but possesses a longer nonlinear region which reaches a plateau at about 3.2% strain. Concerning 3D 4-directional braided composites, the shear stress-strain curve of uncut specimen shows an initial elastic phase up to about 0.8% strain and a nonlinear region which reaches the peak value at about 2.6% strain. In contrast, the shear stress-strain curve of cut specimen shows a smaller initial elastic phase up to less than 0.5% strain followed with a longer nonlinear region which reaches a plateau at about 2.7% strain.

4.3.2. Shear properties

The shear properties of the four configurations are presented in

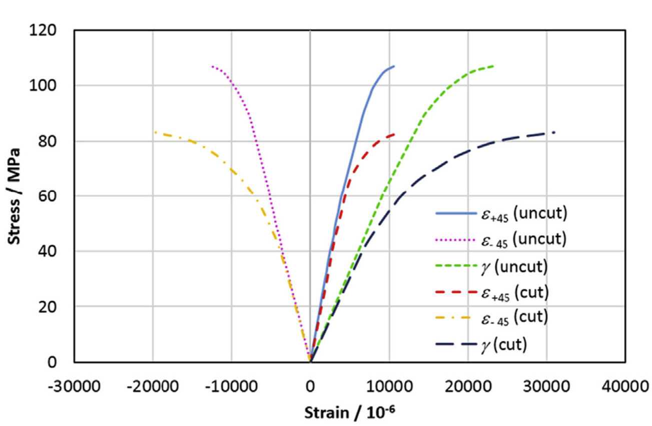

Fig. 12. In-plane shear stress-strain curves of 3D surface-core braided composites.

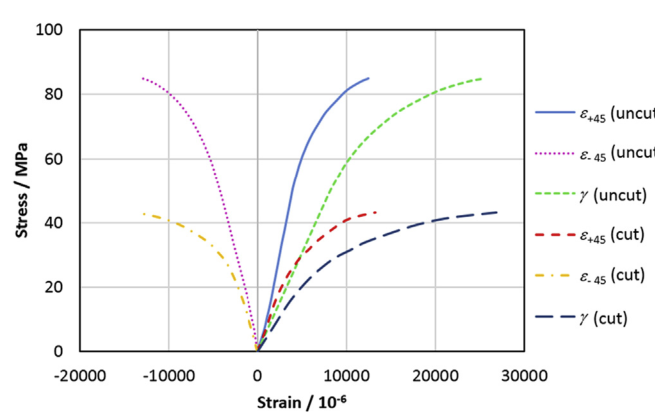

Fig. 13. In-plane shear stress-strain curves of 3D 4-directional braided composites.

Table 2
Average shear modulus and shear strength.

Sample	Braiding angle (°)	Fiber volume fraction (%)	Shear modulus (GPa)	Shear strength (MPa)
MU	35	43	6.600	107.291
MC	–	–	6.070	83.758
TU	32	42	6.111	85.456
TC	–	–	4.245	43.873

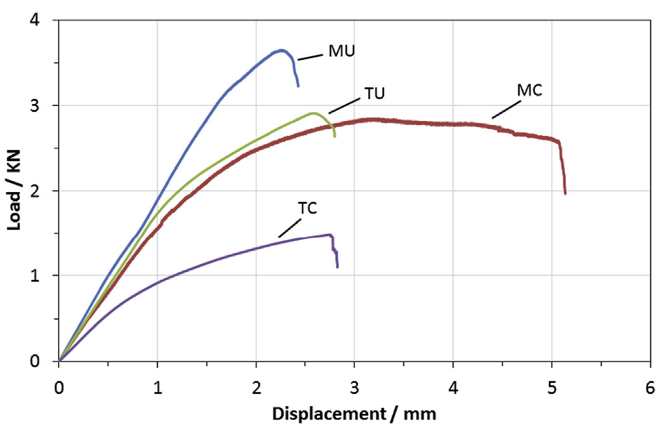

Fig. 14. Load-displacement curves of uncut and cut specimens for 3D surface-core and 3D 4-directional braided composites.

Table 2. *MU* and *MC* represent uncut and cut 3D surface-core braided composites; *TU* and *TC* denote uncut and cut 3D 4-directional braided composites. The shear moduli were calculated over a 0.1–0.4% shear strain range. With similar braiding angles and fiber volume fractions, the average shear moduli of uncut specimens for 3D surface-core braided composites (6.600 GPa) and 3D 4-directional braided composites (6.111 GPa) differ not obviously while those of cut specimens for the two materials show a distinct difference (6.070 GPa and 4.245 GPa). By comparison, the modulus decline of 3D surface-core braided composites caused by surface cuttings is significantly smaller. The shear strengths of the two materials also have different response to surface cuttings. The average shear strength of 3D surface-core braided composites drops from 107.291 MPa to 83.758 MPa while that of 3D 4-directional braided composites drops from 85.456 MPa to 43.873 MPa. Obviously, the latter is more sensitive to surface cuttings.

It is seen from above that surface cuttings degrade the shear properties of both the 3D surface-core and 3D 4-directional braided composites, but the influences are distinct. The average shear modulus and strength of 3D surface-core braided composites drop 8 and 22% while those of 3D 4-directional braided composites drop 31 and 49%. Consequently, the new material possesses relatively better cutting resistance and effectively restrains the degradation of shear properties.

The shear responses of the two braided composites including the cut and uncut specimens are presented by the axial load-displacement curves as shown in Fig. 14. Since the shear properties of each specimen in the same configuration fluctuate slightly, one of the six specimens is demonstrated for all cases. Comparing the curves of uncut and cut specimens for the two materials respectively, the initial gradient and peak load of 3D 4-directional braided composites decrease more severely than those of 3D surface-core braided composites do, which reflects that the modulus and strength of the former degrade more seriously. By surface cuttings, *MC* and *TC* earlier go into the yield phases and later reach the peak values than *MU* and *TU* do. When reaching the peak value, *MC* undergoes a certain stationary phase while other curves directly fall. Compared with *MU*, *MC* shows a more ductile load-displacement response with a larger failure deformation.

4.3.3. Failure modes

The typical failure modes of the four configurations are shown in Fig. 15. For both the 3D surface-core and 3D 4-directional braided composites, only the uncut specimens fail with shear fractures. Possessing relatively intact fiber architectures, the uncut specimens can fully mobilize their own carrying capacity, and bear higher shear loads. From Fig. 15(a) and (b), the fracture surfaces with broken fibers are produced in the shear areas. The white regions close to the failure sections indicate the matrix shear failure.

The fracture morphologies of uncut specimens were observed by scanning electron microscopy (SEM) to reveal their distinct in-plane shear damage mechanisms. Fig. 16(a) shows the fracture structure of 3D surface-core braided composite. It is seen that the broken yarns are still kept in bunches, and their fibers are bonded relatively well. From Fig. 16(b), plenty of flat fracture surfaces of fibers are observed, indicating that these fibers are fractured in a

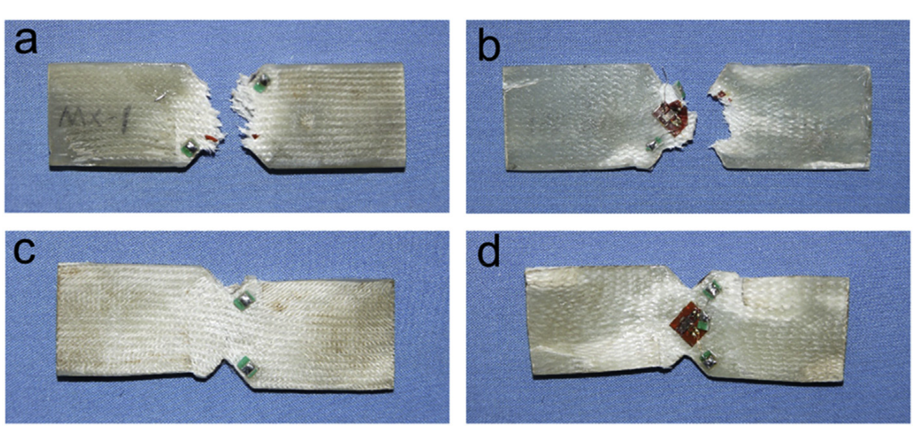

Fig. 15. Failure modes of uncut and cut specimens for 3D surface-core and 3D 4-directional braided composites.

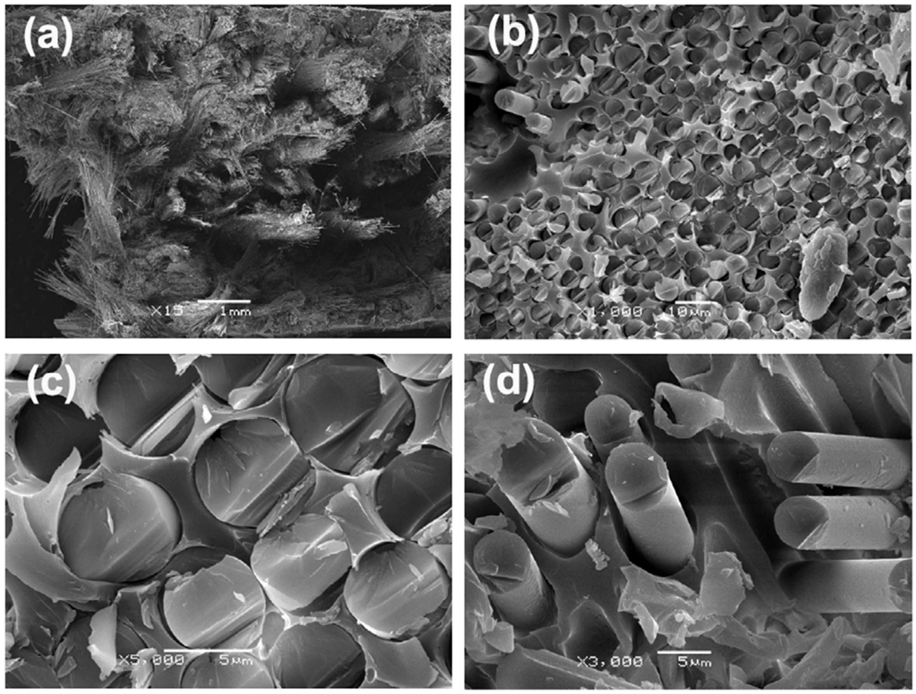

Fig. 16. In-plane shear fracture morphologies of 3D surface-core braided composites: (a) fracture surface at low magnification, (b) fibers fracture and pullout, (c) fibers brittle fracture and (d) fibers ductile fracture.

brittle manner. Since the fiber distribution and orientation in braided composites change greatly, the stress transfer is quite complex. When some microcrack tips perpendicular to the fibers possess focusing energy, the fibers can be impacted. Once enough energy is focused on the micro-crack tips, the vicinal fibers may break for the chain, which can cause the composites brittle failure. Due to the smaller bonding strength in the fiber/matrix interface than the ultimate strength of the matrix, slight interfacial debonding between fibers and matrix occurs in the fiber bundles, as shown in Fig. 16(c). Besides, a few pullout fibers are also observed in Fig. 16(b). The fibers pullout is closely related to the interface sliding stress which is produced during the shear load transfer from matrix to fibers. When the interface sliding stress is high enough to overcome the friction resistance and the bonding strength of fiber/matrix is weak, the fibers will be easily pulled out and will finally produce ductile fractures, as shown in Fig. 16(d).

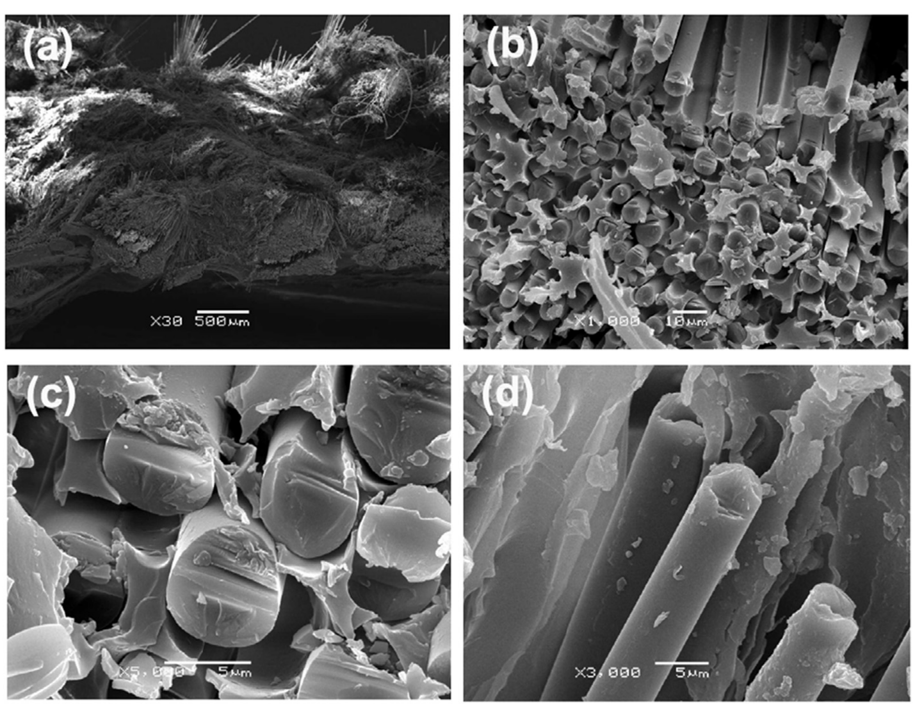

Fig. 17. In-plane shear fracture morphologies of 3D 4-directional braided composites: (a) fracture surface at low magnification, (b) fibers fracture and pullout, (c) fibers brittle fracture and (d) fibers ductile fracture.

In comparison, the broken yarns of 3D 4-directional braided composite are relatively incompact on the fracture surface, leaving end fibers radial distribution, as shown in Fig. 17(a). A large number of pullout fibers are observed in Fig. 17(b) indicating the ductile fractures are relatively common for the present braided composite. Meanwhile, the brittle fracture sections of fibers can also be found, accompanied by serious interface crack, as shown in Fig. 17(c). During the loading process, the difference of strains between the fibers and matrix is remarkable, which leads to high interfacial shear stress. The interface accordingly produces certain plastic deformations and stress concentrations, and is finally cracked. The microcracks propagate on the fiber/matrix interface, and separate the matrix from the fibers. Further crack growth and coalescence disintegrate the matrix and make it drop from the fiber bundles, as shown in Fig. 17(d).

The cut specimens of the two materials fail without shear fractures but both produce relatively larger failure deformations, as shown in Fig. 15(c) and (d). However, these deformations come from different failure mechanisms of the two structures. Surface cuttings break all braiding yarns of 3D 4-directional braided composites, which severely damages the structural integrity and makes the spatial fiber network much looser. Therefore the bearing capacity of the specimen obviously declines, and the shear deformation can be easily produced. As the shear deformation increases, the specimen yields soon, and then the load goes up more and more slowly, maintaining at relatively low levels all along. Finally, the specimen unloads, leaving a certain failure deformation. For 3D surface-core braided composites, surface cuttings break the surface-cores perpendicular to the specimen surface, while the remaining ones parallel to it still maintain their integrality and the fiber architecture is not completely destroyed. These intact surface-cores well preserve their carrying capacity, thus the applied load can reach relatively high levels, which subsequently brings the specimen corresponding deformation. Meanwhile, the damages of those surface-cores perpendicular to the specimen surface may cause the specimen certain normal deformations in the local regions. Under the high load, the shear area of specimen warps slightly, which further intensifies the failure deformation.

5. Conclusion

RVE models are established to study the in-plane shear properties of 3D surface-core braided composite by using finite element method. The numerical results indicate that the surface-cores parallel to material surface bear primary shear load by producing tensile or compressive axial stress in the fibers while the surface-cores perpendicular to material surface are insensitive to the load. Then the basic shear properties affected by braiding angle and fiber volume fraction are obtained by adopting homogenization approach and volume averaging method. In-plane shear properties of undamaged and pre-damaged 3D surface-core and 3D 4-directional braided composites are respectively measured by Arcan method. The experimental data show that 3D surface-core braided composites possess better performance to restrain the degradation of shear properties caused by surface cuttings. For both the materials, only the uncut specimens fail with fractures while the cut ones fail leaving larger shear deformations. The fracture surfaces are observed by scanning electron microscopy (SEM), and the corresponding failure mechanisms of the two materials are identified.

Acknowledgements

The work is partially supported by the National Natural Science Foundation of China (No. 11272147), the State Key Laboratory Program (0214G02) and the Priority Academic Program Development of Jiangsu Higher Education Institutions.

References

[1] A.P. Mouritz, M.K. Bannister, P.J. Falzon, K.H. Leong, Review of applications for advanced three-dimensional fibre textile composites, Compos. Part A 30 (1999) 1445–1461.
[2] K. Xu, X.M. Qian, Analytical prediction of the elastic properties of 3D braided composites based on a new multiunit cell model with consideration of yarn distortion, Mech. Mater. 92 (2016) 139–154.
[3] Y.Q. Wang, A.S.D. Wang, Microstructure/property relationships in three dimensionally braided fiber composites, Compos. Sci. Technol. 53 (1995) 213–222.
[4] J.W. Dong, N.F. Huo, A two-scale method for predicting the mechanical properties of 3D braided composites with internal defects, Compos. Struct. 152 (2016) 1–10.
[5] Y.M. Wan, Y.J. Wang, B.H. Gu, Finite element prediction of the impact compressive properties of three-dimensional braided composites using multi-scale model, Compos. Struct. 128 (2015) 381–394.
[6] D.S. Li, Z.X. Lu, L. Chen, J.L. Li, Microstructure and mechanical properties of three dimensional five-directional braided composites, Int. J. Solids Struct. 46 (17–18) (2009) 3422–3432.
[7] D.S. Li, Z.X. Lu, N. Jiang, D.N. Fang, High strain rate behavior and failure mechanism of three-dimensional five-directional carbon/phenolic braided composites under transverse compression, Compos. Part B Eng. 42 (2) (2011) 309–317.
[8] W.J. Na, H.C. Ahn, S.Y. Jeon, J.S. Lee, H.M. Kang, W.R. Yu, Prediction of the braid pattern on arbitrary-shaped mandrels using the minimum path condition, Compos. Sci. Technol. 91 (2014) 30–37.
[9] S. Kazemahvazi, N. Khokar, S. Hallstrom, H.N.G. Wadley, V.S. Deshpande, Confluent 3D-assembly of fibrous structures, Compos. Sci. Technol. 127 (2016) 95–105.
[10] W.F. Hao, Y.N. Yuan, X.F. Yao, Y.J. Ma, Computational analysis of fatigue behavior of 3D 4-directional braided composites based on unit cell approach, Adv. Eng. Softw. 82 (2015) 38–52.
[11] W.W. Zuo, L.Y. Xiao, D.X. Liao, Statistical strength analyses of the 3-d braided composites, Compos. Sci. Technol. 67 (2007) 2095–2102.
[12] X.Y. Pei, L. Chen, J.L. Li, Y.H. Tang, K.F. Chen, Effect of damage on the vibration modal of a novel three-dimensional and four-directional braided composite T-beam, Compos. Part B Eng. 86 (2016) 108–119.
[13] H.L. Zhou, Z.X. Pan, R.K. Gideon, B.H. Gu, B.Z. Sun, Experimental and numerical investigation of the transverse impact damage and deformation of 3-D circular braided composite tubes from meso-structure approach, Compos. Part B Eng. 86 (2016) 243–253.
[14] J.L. Li, Y.N. Jiao, Y. Sun, L.M. Wei, Experimental investigation of cut-edge effect on mechanical properties of three-dimensional braided composites, Mater. Des. 28 (2007) 2417–2424.
[15] J. Sun, G.M. Zhou, C.W. Zhou, Microstructure and mechanical properties of 3D surface-core 4-directional braided composites, J. Mater. Sci. 50 (2015) 7398–7412.
[16] E.H. Rani, H.A. Rami, In-plane shear testing of thick-section pultruded FRP composites using a modified Arcan fixture, Compos. Part B Eng. 35 (2004) 421–428.
[17] D.O. Adams, J.M. Moriarty, A.M. Gallegos, D.F. Adams, The v-notched rail shear test, J. Compos. Mater. 41 (3) (2007) 281–297.
[18] H.B. Guo, B. Wang, P.R. Jia, C.P. Yang, In-plane shear behaviours of a 2D-SiC/SiC composite under various loading conditions, Ceram. Int. 41 (2015) 11562–11569.
[19] Y. Liang, H. Wang, X.S. Gu, In-plane shear response of unidirectional fiber reinforced and fabric reinforced carbon/epoxy composites, Polym. Test. 32 (2013) 594–601.
[20] L. Li, Y. Zhao, H. Vuong, Y. Chen, J. Yang, Y.X. Duan, In-plane shear investigation of biaxial carbon non-crimp fabrics with experimental tests and finite element modeling, Mater. Des. 63 (2014) 757–765.
[21] A.C. Manalo, T. Aravinthan, W. Karunasena, In-plane shear behaviour of fibre composite sandwich beams using asymmetrical beam shear test, Constr. Build. Mater. 24 (2010) 1952–1960.
[22] C.C. Chamis, Mechanics of composites materials: past, present and future, J. Compos. Technol. Res. 11 (1) (1989) 3–14.
[23] A.S. Jarvis, Meso-Scale and Multicontinuum Modeling of a Triaxial Braided Textile Composite, University of Wyoming, Laramie, 2009.
[24] P. Qu, X.J. Guan, Y.X. Jia, S. Lou, J.Q. Nie, Effective elastic properties and stress distribution of 2D biaxial nonorthogonally braided composites, J. Compos. Mater. 46 (8) (2011) 997–1008.
[25] W. Yang, Meso-mechanics and meso-damage mechanics, Adv. Mech. 22 (1992) 1–9 (in Chinese).
[26] K. Xu, X.W. Xu, Finite element analysis of mechanical properties of 3D five-directional braided composites, Mater. Sci. Eng. A 487 (1–2) (2008) 499–509.
[27] C. Zhang, X.W. Xu, Finite element analysis of 3D braided composites based on three unit-cells models, Compos. Struct. 98 (2013) 130–142.